

Magnetic ground state, critical analysis of magnetization, and large magnetocaloric effect in the ferromagnetically coupled kagome lattice $\text{YCa}_3(\text{MnO})_3(\text{BO}_3)_4$

A. Choudhary,¹ A. Magar,¹ S. Ghosh,² S. Kanungo,² and R. Nath^{1,*}

¹*School of Physics, Indian Institute of Science Education and Research Thiruvananthapuram-695551, India*

²*School of Physical Sciences, Indian Institute of Technology Goa-403401, India*

We report a detailed study of the magnetic properties, critical analysis of magnetization, and magnetocaloric effect of a spin-2 kagome lattice $\text{YCa}_3(\text{MnO})_3(\text{BO}_3)_4$. The experiments are complemented by the density functional band structure calculations. The magnetic measurements suggest a highly frustrated nature of the compound due to competing ferro- and antiferromagnetic interactions with the dominant one being ferromagnetic. It undergoes a unconventional ferromagnetic ordering at $T^* \simeq 7.8$ K and a field induced metamagnetic transition in low fields, implying spin canting. A H - T phase diagram is constructed that features three phase regimes. Indeed, the band structure calculations reveal dominant ferromagnetic interaction along the chains that are coupled antiferromagnetically yielding a frustrated kagome geometry. This compound shows a large magnetocaloric effect with isothermal entropy change $\Delta S_m \simeq 12$ J/kg-K, adiabatic temperature change $\Delta T_{ad} \simeq 8.4$ K, and relative cooling power $RCP \simeq 349$ J/kg for a field change of 7 T. The critical analysis of magnetization and magnetocaloric parameters suggests that the transition is a second order phase transition and it is tricritical mean field type. Owing to its large magnetocaloric parameters, second order phase transition, and no thermal hysteresis, $\text{YCa}_3(\text{MnO})_3(\text{BO}_3)_4$ emerges as a potential rare-earth free material for magnetic refrigeration.

I. INTRODUCTION

For decades, geometrically frustrated magnets in two-dimension have lured enormous attention, especially to explore the exotic phases of matter [1]. A classic example of the 2D frustrated magnet is the kagome lattice, composed of corner-shared triangles with coordination number four [2]. The kagome lattices with Heisenberg antiferromagnetic (AFM) interaction and low spin values set a perfect avenue to realize quantum spin liquid (QSL), a highly entangled quantum state with no magnetic long-range order (LRO). Indeed, it is experimentally observed in well celebrated $S = 1/2$ kagome lattice compounds like herbertsmithite $[\text{ZnCu}_3(\text{OH})_6\text{Cl}_2]$ [2, 3]. Subsequently, the endeavor to realize spin-liquid and other fascinating phenomenon has also been made in kagome lattices with high spin ($S > 1/2$). For instance, the $S = 5/2$ jarosite compounds, $\text{AFe}_3(\text{OH})_6(\text{SO}_4)_2$ feature a spin-glass transition for $A = (\text{H/D})_3\text{O}$ and an antiferromagnetic ordering for $A = \text{Na}$ and K [4–7]. On the contrary, muon spin relaxation (μSR) study on $S = 3/2$ jarosite compound $\text{KCr}_3(\text{OH})_6(\text{SO}_4)_2$ reveals a clear signature of persistent spin fluctuations down to 25 mK [8]. Oddity with other jarosites, $S = 1$ jarosite compounds $M\text{V}_3(\text{OH})_6(\text{SO}_4)_2$ ($M = \text{Na}, \text{Rb}, \text{Ag}, \text{Tl}, \text{and } \text{NH}_4$) have strong ferromagnetic interactions [9]. In the $S = 2$ kagome compound $\text{CsMn}_3\text{F}_6(\text{SeO}_3)_2$, the electron spin resonance and μSR experiments reveal a cooperative paramagnetic behavior down to 0.3 K, despite a large Curie-Weiss temperature of ~ 49 K [10].

Generally, more attention is focused on the kagome AFMs because of the quest for a QSL state, but kagome

ferromagnets (FM) also have equally interesting aspects to look for. The kagome FMs demonstrate anomalous Hall effect, Nernst effect, and chiral edge state in several intermetallic compounds [11–13]. The insulating kagome FM is also predicted to demonstrate topologically non-trivial bands [14]. The experimental realization of flat magnon band and magnon Hall effect is reported only in the insulating $S = 1/2$ kagome ferromagnet $\text{Cu}[1,3\text{-bdc}]$ [15, 16]. Therefore, despite non-frustrated nature, kagome ferromagnets hold promise in elucidating many fundamental aspects of magnetism and corroborating the theoretical predictions.

Moreover, kagome ferromagnets are also of increasing demand as magnetocaloric effect (MCE) candidates [17]. MCE is a green-energy and cost-effective solution in refrigeration in the sub-kelvin range over conventional cryogenics like liquid helium and nitrogen. Magnetic cooling down to sub-kelvin temperatures can be achieved by adiabatic demagnetization of materials having a giant MCE [18]. For efficient cooling, the material should exhibit a large isothermal entropy change for a small change in magnetic field at low temperatures and negligible magnetic hysteresis [19]. Therefore, ferromagnetic insulators with second-order phase transition can be excellent MCE materials for cooling to low temperatures. The mineral gaufreyite $\text{Ca}_4(\text{MnO})_3(\text{BO}_3)_3\text{CO}_3$ is a rare example of naturally occurring perfectly kagome lattice. It has dominant ferromagnetic (FM) interactions and undergoes a glassy transition below $T_f \simeq 10$ K [20]. Additionally, it is reported to be an excellent MCE candidate for hydrogen liquification [20]. Subsequently, a derivative of gaufreyite, $\text{YCa}_3(\text{MO})_3(\text{BO}_3)_4$, ($M = \text{Cr}, \text{Mn}, \text{V}$) family has been synthesized. They crystallise in a hexagonal crystal structure with $P6_3/m$ space group. The Cr analogue ($S = 3/2$) doesn't show any magnet LRO down to 2 K [21]. Similarly, the V analogue ($S = 1$) also exhibits a

* rnath@iisertvm.ac.in

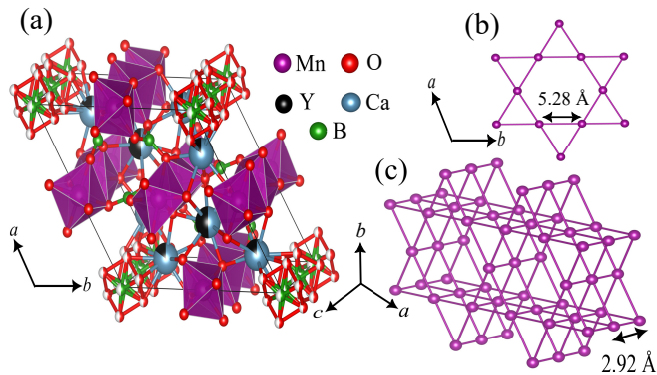


FIG. 1. (a) Unit cell of YCMBO featuring edge-shared MnO_6 octahedra. (b) A single kagome motif in the ab -plane made up of equilateral triangular units. (c) Two kagome planes separated by a relatively small distance of 2.92 Å, showing the formation of Mn^{3+} chains along the c -axis.

broad dispersionless excitation without a magnetic LRO down to 50 mK [22, 23]. Interestingly, both compounds have very large Curie-Weiss temperature, characterizing them as highly frustrated magnets. On the other hand, the Mn analogue $[\text{YCa}_3(\text{MnO})_3(\text{BO}_3)_4]$ is reported to undergo a non-trivial FM ordering below 7.5 K [24]. The neutron powder diffraction experiments suggested that it is composed of edge-sharing ferromagnetic chains of MnO_6 octahedra along the c -axis which are interconnected antiferromagnetically via BO_3 groups to form a kagome lattice in the ab -plane. Below 7.5 K, the magnetic moments of the chains order to give a normal $q = 0$ structure.

In this work, we present a detailed magnetic and magnetocaloric properties of a kagome ferromagnet $\text{YCa}_3(\text{MnO})_3(\text{BO}_3)_4$ (YCMBO). In the crystal structure, as shown in Fig. 1, the MnO_6 octahedra are connected through BO_3 units to form a perfect kagome lattice in the ab -plane. The kagome layers are closely stacked via edge-sharing of MnO_6 octahedra forming continuous chains along the c -axis. While the interaction along the chain is found to be FM, the AFM interchain interaction constitute a kagome lattice. Along with a FM ordering at $T^* \simeq 7.8$ K, magnetization reveals a field induced metastable transition. It exhibits a large MCE comparable to other MCE materials having the transition temperature at around T^* . We also did a detailed critical analysis of magnetization and MCE parameters, establishing the second order nature and universality class of the phase transition.

II. METHODS

A polycrystalline sample of YCMBO was prepared by the conventional solid-state reaction method. The starting materials used in this reaction were Mn_2O_3 (Sigma Aldrich, 99.9 %), Y_2O_3 (Sigma Aldrich, 99.99%), CaCO_3 (Sigma Aldrich, 99.9%), and H_3BO_3 (Sigma Aldrich,

99.9%). First, Y_2O_3 and CaCO_3 were pre-heated at 500°C for 6 hrs. Subsequently, the precursors taken in stoichiometric ratios were ground thoroughly and pressed into pellets. In order to compensate the loss of B in the high temperature synthesis, H_3BO_3 was taken 5% extra. The pressed pellets were first fired at 900°C for 24 hrs, followed by multiple firings at 1000°C for 24 hrs each with intermediate grindings.

The phase purity of the polycrystalline sample was confirmed from powder x-ray diffraction (XRD) using PANalytical Xpert-Pro diffractometer ($\text{Cu } K_\alpha$ radiation with $\lambda_{av} = 1.54182$ Å). The obtained powder XRD data is presented in Fig. 2 along with the Rietveld fit. The Rietveld refinement was done using the FullProf software package, and initial structural parameters were adopted from the previous report [24]. The refined lattice parameters $a = b = 10.553(8)$ Å, $c = 5.847(7)$ Å, $\alpha = \beta = 90^\circ$, and $\gamma = 120^\circ$ are in good agreement with the previous report. The absence of any extra peak and the reduced value of the goodness of fit ($\chi^2 \sim 2.9$) confirm the phase purity of the synthesized polycrystalline sample. The refined atomic co-ordinates are shown in Table I.

DC magnetization (M) as a function of temperature (T) and magnetic field (H) was measured using a superconducting quantum interference device (SQUID) (MPMS-3, Quantum Design) magnetometer in the T -range of 1.8 K to 380 K and in magnetic field up to 7 T. AC susceptibility was measured as a function of temperature ($2 \text{ K} \leq T \leq 100 \text{ K}$) and frequency ($100 \text{ Hz} \leq \nu \leq 10 \text{ kHz}$) in an AC field of 5 Oe using the ACMS option of the PPMS. Heat capacity (C_p) as a function of temperature ($2 \text{ K} \leq T \leq 300 \text{ K}$) was measured on a small sintered pellet using the thermal relaxation technique in PPMS in different applied fields from 0 to 7 T.

The Electron Spin Resonance (ESR) experiments were performed using a Bruker EMX-series-X-band spectrometer ($\nu = 9.4$ GHz). The sweeping of the magnetic field under a continuous microwave irradiation yields the ESR signal, which is recorded as the first field derivative of the absorbed microwave power dP/dH as a function of the field.

The first-principles electronic structure calculations were carried out within the framework of density functional theory (DFT) employing the projector augmented-wave (PAW) method [25, 26] and the generalized gradient approximation (GGA) in the Perdew-Burke-Ernzerhof (PBE) formulation [27] for the exchange-correlation functional, as implemented in the plane-wave-based Vienna Ab-initio Simulation Package (VASP) [25, 26]. A kinetic energy cutoff of 500 eV was used for the plane-wave basis set, which ensured convergence of the total energy. Structural optimization was performed by relaxing the internal atomic positions while maintaining the experimentally determined lattice parameters. The Mn atoms, occupying high-symmetry Wyckoff positions (6g), were constrained during relaxation using the selective dynamics scheme. The PBEsol [28] functional was employed to improve the description of equilibrium

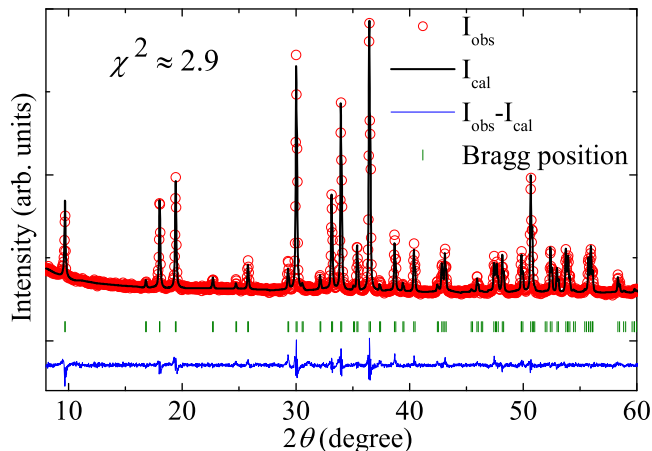


FIG. 2. Powder XRD data (circles) with the Rietveld fit (black solid line) of the titled compound. Bragg positions are shown as green vertical bars, and the bottom line indicates the difference between experimental and calculated intensities.

structural properties, with convergence thresholds set to 10^{-5} eV for total energy and 10^{-3} eV/Å for the maximum Hellmann–Feynman force on each atom.

To incorporate on-site electronic correlations beyond standard GGA, the GGA+ U approach [29, 30] was employed using an effective Hubbard parameter of $U_{\text{eff}} = (U - J_H) = 5$ eV for the Mn- d orbitals. The self-consistent calculations were performed with a stringent energy convergence criterion of 10^{-7} eV. The Brillouin zone (BZ) integration was performed using a $6 \times 6 \times 10$ Monkhorst–Pack k -point mesh. The effect of spin–orbit coupling (SOC) was included via relativistic corrections to the pristine Hamiltonian [31]; however, its influence on the electronic structure was found to be negligible for the present system. In addition to the electronic structure analysis, Bader charge analysis [32, 33] was performed using the charge density from the converged self-consistent calculations to confirm the charge state of each atom.

III. RESULTS AND DISCUSSION

A. Magnetization

Temperature variation of magnetic susceptibility χ ($\equiv M/H$) measured in different applied magnetic fields is shown in Fig. 3(a). As the temperature decreases, χ increases systematically and shows a peak at $T^* \simeq 7.8$ K for $\mu_0 H = 0.5$ T, indicating a transition from paramagnetic to an ordered state. The peak-like feature shifts to lower temperatures with increasing field and becomes very broad above 2 T. To access the nature of interactions, we have plotted χT vs T in the inset of Fig. 3(a). χT first increases, passes through a broad maximum, and then decreases towards low temperatures. This behavior points towards the presence of coexisting FM and AFM interactions in YCMBO [34, 35]. This is indeed consis-

TABLE I. The Wyckoff positions, atomic coordinates, and occupancy of individual atoms in YCMBO, obtained from the Rietveld refinement of the powder XRD.

Atomic sites	Wyckoff positions	x	y	z	Occ
Mn	6g	0.5	0	0	1
Y(1)	2c	0.333(3)	0.666(7)	0.25	0.51
Y(2)	6h	0.120(6)	0.837(9)	0.25	0.16
Ca(1)	2c	0.333	0.666(1)	0.25	0.49
Ca(2)	6h	0.120(6)	0.837(9)	0.25	0.84
B(1)	6h	0.226(6)	0.789(6)	0.75	1
B(2)	4e	0	0	0.693	0.5
O(1)	6h	0.086(5)	0.464(3)	0.25	1
O(2)	6h	0.315(1)	0.919(5)	0.75	1
O(3)	12i	0.299(1)	0.470(9)	0.547(6)	1
O(4)	12i	0.058(9)	0.914(2)	0.581(7)	0.5

tent with the findings from neutron diffraction experiments reported earlier [24].

To extract the magnetic parameters, $1/\chi$ vs T data in the high temperature regime ($T \geq 150$ K) were fitted by the Curie-Weiss (CW) law

$$\chi(T) = \chi_0 + \frac{C}{(T - \theta_{\text{CW}})}, \quad (1)$$

where χ_0 is the T -independent susceptibility, C is the Curie constant, and θ_{CW} is the characteristic Curie-Weiss temperature. The fit shown in Fig. 3(b) gives $\chi_0 \simeq -1.6 \times 10^{-4}$ cm³/mol-Mn³⁺, $C \simeq 3.04$ cm³K/mol-Mn³⁺, and $\theta_{\text{CW}} \simeq 34$ K. The fitting parameter C gives the effective magnetic moment of $\mu_{\text{eff}} \simeq 4.93 \mu_B$ which is close to the spin only effective moment of Mn³⁺ ($S = 2$) ion [$(\mu_{\text{eff}})_{\text{theory}} = 4.89 \mu_B$], assuming $g = 2$. Indeed, our ESR experiment (discussed later) yield $g \sim 2$. According to mean-field theory, θ_{CW} is the sum of all exchange couplings in the system. Thus, the large and positive value of θ_{CW} for YCMBO indicates that the dominant interaction is FM in nature. Further, $T^* \sim 7.8$ K is considerably suppressed compared to θ_{CW} , yielding a frustration ratio of $f = \frac{|\theta_{\text{CW}}|}{T^*} \simeq 4$. Such a value of f is usually considered as moderate frustration in an AFM system. However, in YCMBO due to competing FM and AFM interactions, the value of θ_{CW} is expected to be reduced, as compared to a purely AFM system [36]. Hence, f does not reflect the actual strength of frustration in such compounds.

χ vs T measured in a small magnetic field of 100 Oe in zero-field-cooled (ZFC) and field-cooled (FC) protocols exhibits a bifurcation below T^* [see Fig. 3(c)]. To scrutinize the possibility of spin-glass below the ordering temperature, we have performed the frequency-dependent AC susceptibility measurements in a small AC field of 5 Oe around T^* , as shown in the inset of Fig. 3(c). The real part of AC susceptibility (χ') shows a peak at T^* , but it is completely frequency independent, suggesting

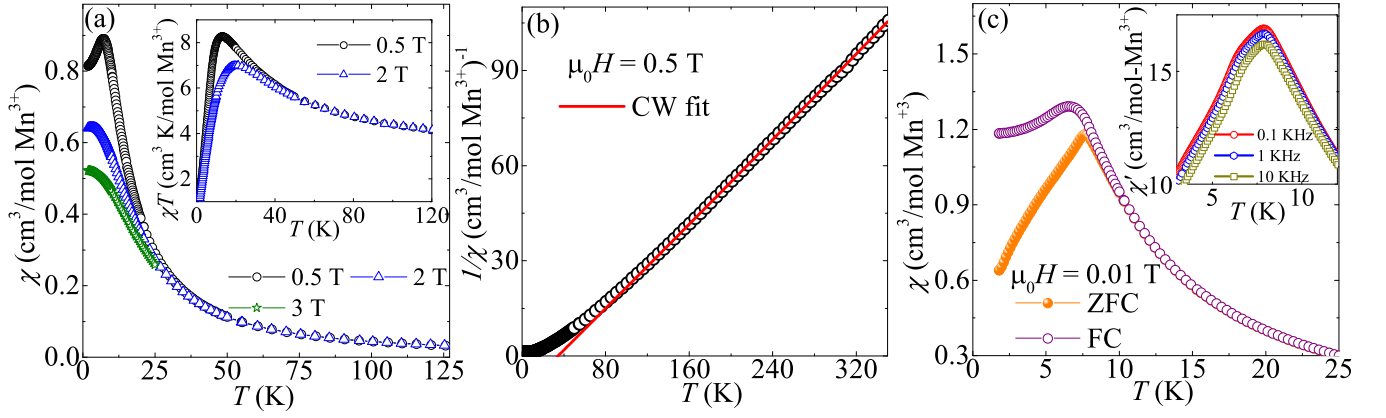


FIG. 3. (a) Magnetic susceptibility (χ) as a function of temperature measured in different applied fields. Inset: χT vs T data. (b) Inverse susceptibility $1/\chi$ vs T along with the CW fit (solid line). (c) $\chi(T)$ measured at $\mu_0 H = 0.02$ T in ZFC and FC protocols. Inset: Real part of AC susceptibility (χ') measured in different frequencies.

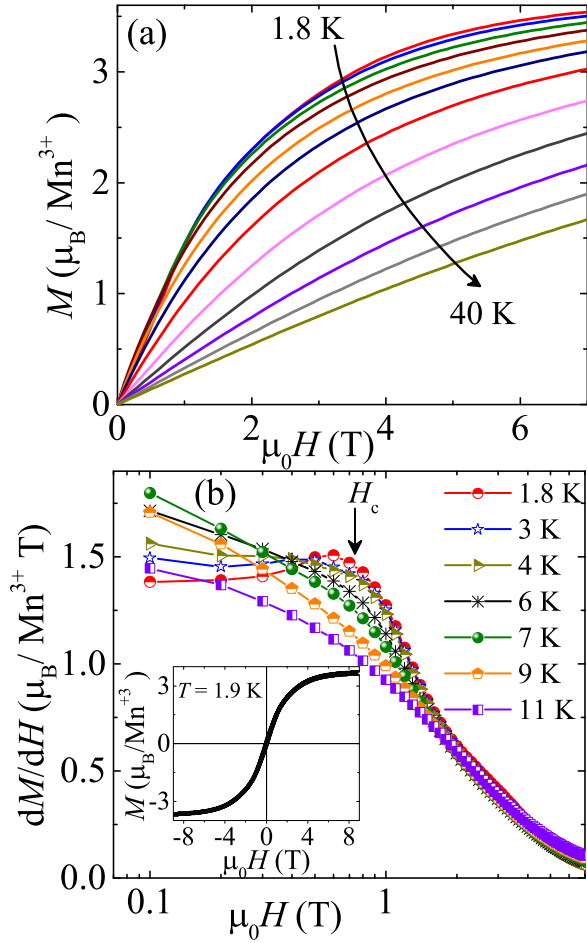


FIG. 4. (a) Isothermal magnetization (M) vs H measured at different temperatures. (b) Temperature evolution of the derivative of magnetization (dM/dH) exhibiting a slope change at low fields. Inset: Complete magnetization isotherm at $T = 1.9$ K, showing saturation magnetization and minuscule hysteresis.

the absence of spin freezing or spin-glass behavior. The bifurcation observed in ZFC and FC $\chi(T)$ might be due to a small amount of disorder in the polycrystalline sample [37].

Figure 4(a) presents isothermal magnetization curves from 1.8 K to 40 K in small temperature steps. A complete M vs H curve at $T = 1.9$ K is shown in the inset of Fig. 4(b). For $T = 1.8$ K, magnetization increases slowly with an increase in field and almost saturates to a value, $M_s \simeq 3.6 \mu_B$ at 7 T, which is close to the expected saturation magnetization for a $S = 2$ system ($M_s = gS\mu_B = 4\mu_B$). Although the magnetization reaches saturation, it is achieved in a relatively large field in contrast to a conventional FM. This suggests that a higher field was required to saturate the AFM interaction. Additionally, there is a slope change at around $\mu_0 H \simeq 0.7$ T, as clearly visible in the dM/dH vs H plot shown in Fig. 4(b). Such a slope change at an intermediate field (H_c) is not envisaged, indicating spin canting due to an AFM interaction competing with dominant FM interaction [35]. Further, the M vs H curve recorded at $T = 1.9$ K doesn't show any hysteresis [inset of Fig. 4(b)], supporting the absence of a glassy component.

B. Electron Spin Resonance

ESR spectra were recorded down to 110 K on the powder sample. Figure 5 presents the actual absorbed microwave power (P_{abs}) as a function of field at three different temperatures. P_{abs} shows a maxima at resonance field (H_{res}). The exact value of H_{res} for each temperature is determined from a Gaussian fit to the spectra (solid line in Fig. 5). The Lande g -factor is then calculated using the resonance condition, $h\nu = g\mu_B H_{\text{res}}$ where, h is the Planck's constant and ν is the resonance frequency corresponding to H_{res} . We found $g \simeq 2$ in the entire measured temperature range as shown in the inset of Fig. 5.

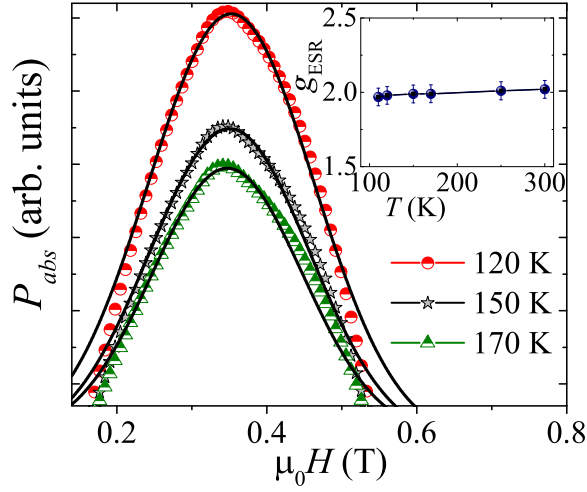


FIG. 5. Absorbed microwave power (P_{abs}) vs H measured at different temperatures. Solid lines are the fits using a Gaussian function. Inset: Variations of g -factor with temperature.

C. Heat Capacity

Temperature dependent heat capacity (C_p) is presented in Fig. 6. The zero-field C_p data exhibit an anomaly at $T^* \simeq 7.5$ K, demonstrating the transition to a magnetic ordered state. YCMBO being a magnetic insulator, the major contributions to C_p are from the magnetic (C_{mag}) and phonon (C_{ph}) parts. The high temperature contribution is mostly C_{ph} while the low temperature contribution is dominant C_{mag} . In order to estimate C_{mag} , one needs to subtract C_{ph} from the total heat capacity. We approximated the phonon contribution by simulating the data by a linear combination of one Debye and four Einstein terms as [38]

$$C_{\text{ph}}(T) = f_{\text{D}} C_{\text{D}}(\theta_{\text{D}}, T) + \sum_{i=1}^4 g_i C_{\text{E}_i}(\theta_{\text{E}_i}, T). \quad (2)$$

The first term in Eq. (2) is the Debye contribution to C_{ph} , which can be written as

$$C_{\text{D}}(\theta_{\text{D}}, T) = 9nR \left(\frac{T}{\theta_{\text{D}}} \right)^3 \int_0^{\frac{\theta_{\text{D}}}{T}} \frac{x^4 e^x}{(e^x - 1)^2} dx. \quad (3)$$

Here, R is the universal gas constant, θ_{D} is the characteristic Debye temperature, and n is the number of atoms in the formula unit. The second term in Eq. (2) gives the Einstein contribution to C_{ph} that has the form

$$C_{\text{E}}(\theta_{\text{E}}, T) = 3nR \left(\frac{\theta_{\text{E}}}{T} \right)^2 \frac{e^{\theta_{\text{E}}/T}}{[e^{\theta_{\text{E}}/T} - 1]^2}. \quad (4)$$

Here, θ_{E} is the characteristic Einstein temperature. The coefficients f_{D} , g_1 , g_2 , and g_3 represent the fraction of atoms that contribute to their respective parts. These values are taken in such a way that their sum should

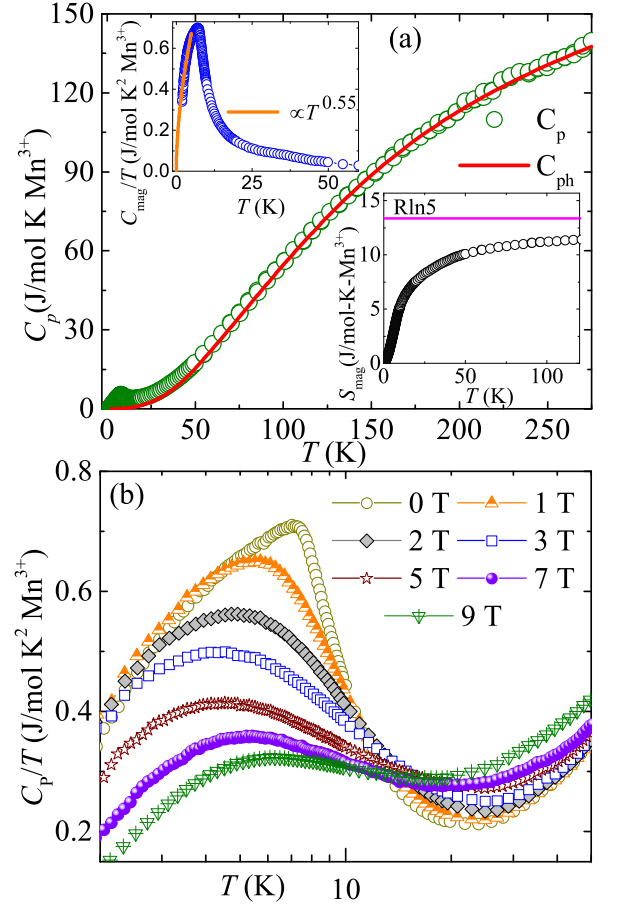


FIG. 6. (a) Heat capacity (C_p) vs T measured in zero-field. The solid line represents the phonon contribution (C_{ph}) determined using the Debye-Einstein model. Upper and lower insets show the magnetic heat capacity (C_{mag}/T) and magnetic entropy (S_{mag}) as a function of temperature in zero-field, respectively. (b) C_p/T vs T in different magnetic fields in the low-temperature regime.

be equal to one. The simulated phonon contribution is shown as a solid line in the main panel of Fig. 6(a) and the obtained C_{mag}/T is plotted as a function of temperature in the upper inset of Fig. 6(a).

The magnetic entropy is calculated as, $S_{\text{mag}}(T) = \int_{0\text{K}}^T \frac{C_{\text{mag}}(T')}{T'} dT' \simeq 11.5$ J/mol-K [see the lower inset of Fig. 6(a)]. It is slightly lower than the expected magnetic entropy for a $S = 2$ system, $S_{\text{mag}} = R \ln 5 = 13.38$ J/mol-K. It is to be noted that only $\sim 40\%$ of the total entropy is released just above T^* and the remaining entropy is released at very high temperatures. This is unlike a conventional FM ordering where the entire entropy is expected to be released just above the transition, suggesting that YCMBO is not a simple FM and has a significant frustration effect. A power law, $C_p = AT^n$ is fitted to C_{mag}/T below 5 K ($< T^*$) that yields $n \simeq 0.5$. Although the value of the exponent is close to the one expected for FM spin wave excitations [39], the ordering is far from a sim-

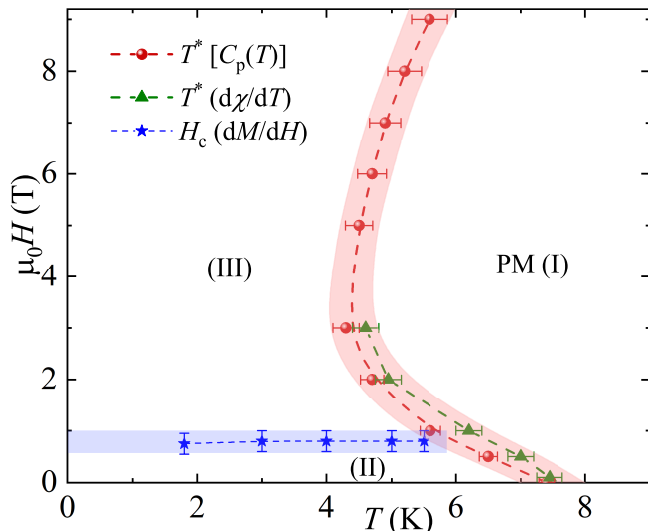


FIG. 7. H - T phase diagram for YCMBO constructed from the magnetization and heat capacity measurements.

ple FM as understood from magnetic entropy and field dependent C_p discussed below.

Figure 6(b) presents C_p/T measured in different applied fields. The zero-field peak initially shifts toward low temperatures, similar to an AFM. With further increase in field (≥ 5 T), the peak becomes very broad and starts shifting to the high temperatures, as expected for a FM. This type of field evolution also supports considerable spin canting in the compound.

D. Phase Diagram

A H - T phase diagram of YCMBO is made by plotting the field dependence of T^* obtained from $\chi(T)$ and $C_p(T)$ measurements along with H_c obtained from the magnetic isotherms. As depicted in Fig. 7, YCMBO undergoes a transition from PM (phase I) to an ordered state (phase II) in zero-field at T^* . As the field increases, T^* moves towards low temperatures in small fields (up to ~ 2 T) and then shifts towards high temperatures in larger fields. Such a behaviour is very unusual and not commonly seen in case of pure ferromagnets. This can possibly be explained in terms of competing FM and AFM interactions. Typically, for a pure FM order, as the field increases, one would expect T^* to shift to high temperatures only. However, in the present case, first, the AFM interaction get suppressed and saturates at about 2 T, leading to a shift of T^* to the low temperature regime. For $H > 2$ T, only the ferromagnetic interaction is influenced, resulting in a outward movement of T^* in higher fields. Further, a field-induced transition H_c is observed in isothermal magnetization that remains temperature independent. Similar field induced phases are typically reported for anisotropic magnets [40]. When plotted together, the phase diagram features three distinct phase regimes (I,

II, and III). Though, such a phase diagram supports the presence of competing FM and AFM interactions, the exact nature of the phases would require further experiments including neutron diffraction in magnetic fields.

E. Electronic Structure Calculations

As mentioned earlier, YCMBO crystallizes in a hexagonal lattice, adopting the well-known gaufroyite-type structure [20], and belongs to the space group $P6_3/m$ (No. 176). Experimental reports indicate a degree of site disorder involving Y, Ca, B, and O atoms; however, for the sake of calculation limitations, a disorder-free configuration with space group $P\bar{6}$ (No. 174) was considered, preserving the chemical stoichiometry intact as that of the experimentally synthesized compound. The crystal structure comprises infinite one-dimensional chains of edge-sharing MnO_6 octahedra extending along the c -axis. The Mn atoms occupy octahedral coordination and exhibit a characteristic Jahn-Teller distortion, with two elongated Mn-O bonds (~ 2.19 Å) and shorter equatorial bonds (~ 1.90 and 1.99 Å). These MnO_6 edge shared chains are bridged by planar triangular BO_3 units, giving rise to a kagome-like network within the ab -plane [see Fig. 8(a)(lower)], as a result, the Mn sublattice forms a kagome lattice in the ab -plane. This kagome geometry introduces geometric frustration, which is central to the material's complex magnetic behavior. The three-dimensional framework formed by MnO_6 octahedra and BO_3 triangles contains tunnel-like interstitial channels running along the c -axis. These voids are occupied by Y and Ca cations, supported by the B and O atoms, contributing towards the stability of the crystal structure.

The spin-polarized density of states (DOS), calculated within the GGA+ U formalism and projected onto Y- s , Ca- p , Mn- d , B- s , and O- p orbitals, is presented in Fig. 8(b). The DOS is plotted over a wide energy window ranging from -8.0 eV below the Fermi level to 8 eV above the Fermi level, relative to the Fermi energy (E_F). Close to the E_F , the Mn- d states dominate, where the majority spin channel states of Mn- d are mostly filled, except a single unoccupied e_g state, while the minority spin channel is completely empty. The calculated magnetic moment at the Mn site is $3.91 \mu_B$ with total magnetic moment $12 \mu_B$ /formula unit. The calculated DOS and magnetic moment together infer that Mn is in +3 oxidation state in the $3d^4$ configuration with high spin $S = 2$ state, as shown in the inset of Fig. 8(b). The Y and Ca are in nominal +3 and +2 oxidation states, with filled shell configurations, respectively. The B and O atoms are calculated to be in the +3 and -2 oxidation states, respectively, consistent with the charge neutrality. Interestingly, we found strong hybridization between O- $2p$ state with the Mn- $3d$ as reflected in the strong overlap of DOS. As a result substantial induced magnetic moment at the oxygen sites. These d - p hybrid states dominate the vicinity of the Fermi level and contribute to the

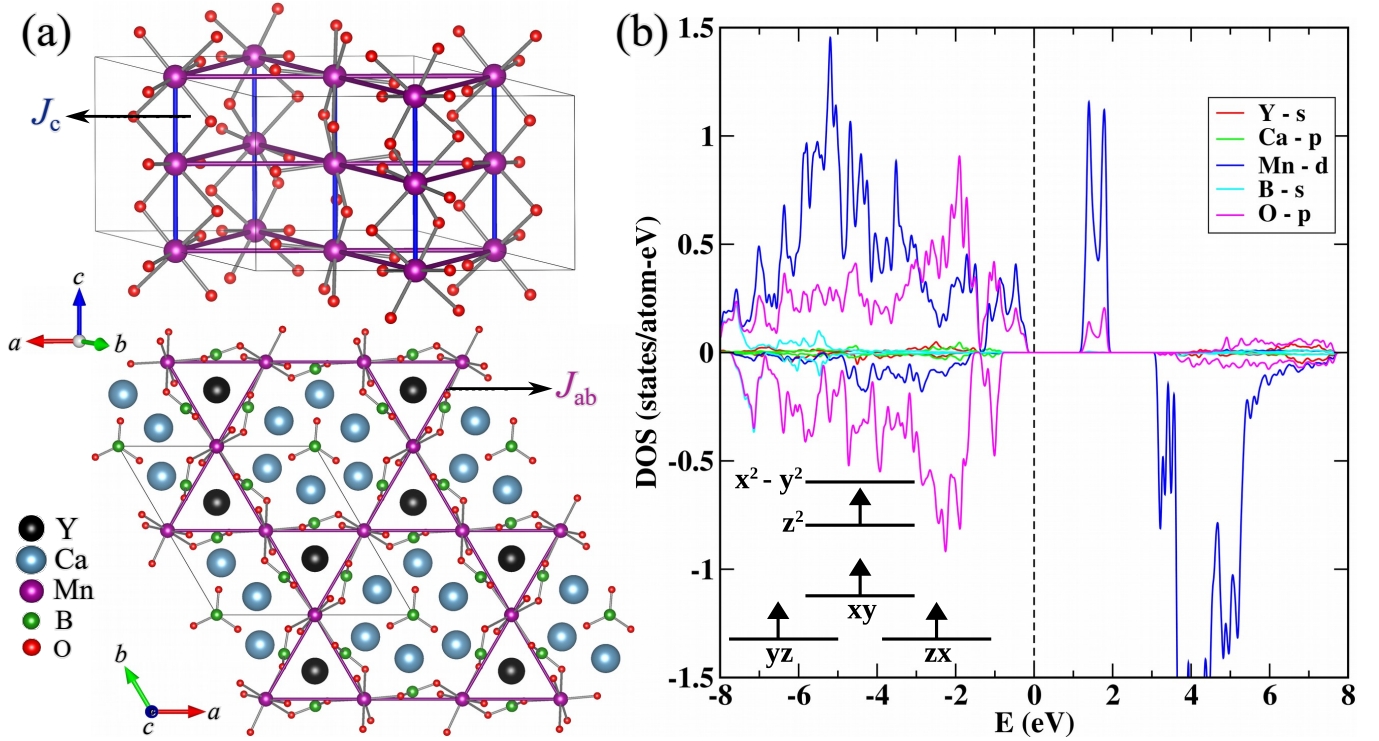


FIG. 8. (a) Three-dimensional crystal structure of YCMBO is shown. Upper and Lower panels show the projection along the crystallographic c -axis and in the ab -plane, respectively, of the bulk structure. Two distinct magnetic exchange interactions between Mn atoms are highlighted (J_c and J_{ab}). (b) Calculated spin-polarized GGA+ U DOS, projected onto atomic orbitals: Y- s , Ca- p , Mn- d , B- s , and O- p states. The energy axis is referenced to the Fermi level ($E_F = 0$ eV). Lower inset: schematic representation of the crystal-field splitting and occupancy of the Mn- d orbitals.

emergence of a band gap of approximately 1.2 eV in the majority spin channel, indicating an insulating ground state, while the contributions from Y, Ca, and B atoms are minimal near the E_F .

As the Mn-sublattice forms an interesting kagome geometry in the ab plane and chains along the c -axis, it is likely to have competition between the quasi-1D vs quasi-2D nature of the magnetic model. We calculated the magnetic ground state via comparative energetics of the FM and AFM spin configurations, and found that FM is energetically lower, thus establishing the FM ground state. Our calculated results are broadly consistent with the earlier report of the observed ferromagnetism in neutron diffraction measurements [24]. To explore further details of the underlying spin model, we went ahead with the calculation of the magnetic exchange interactions between different Mn sites. For the sake of simplicity and to extract the essence of the spin model, we consider two exchange paths, intra-plane coupling (J_{ab}) and out-of-plane i.e., intra-chain coupling (J_c), as shown in Fig. 8(a). J_c is along the MnO_6 chains with Mn-Mn distance ~ 2.93 Å while J_{ab} is across the kagome layers where Mn-Mn distance is ~ 5.28 Å.

There are various methods to calculate the magnetic exchange interaction at the *ab-initio* level. We have adopted the total energy method [41–43], where the DFT

total energies of the different spin configurations are mapped to the corresponding Ising model with two exchange interactions, as shown in the model Hamiltonian

$$H = J_c \sum_{\langle i, c \rangle} \mathbf{S}_i^z \mathbf{S}_{i+c}^z + J_{ab} \sum_{\langle i, ab \rangle} \mathbf{S}_i^z \mathbf{S}_{i+ab}^z. \quad (5)$$

Here, \mathbf{S}^z is the z^{th} component of the spin operator, $\langle i, c \rangle$ and $\langle i, ab \rangle$ denote summation over nearest-neighbor spins along the chain and in the ab -plane, respectively. Although this method has a dependency on the exchange-correlation functional, choice of U , however, this method is successful in providing a qualitative estimate and understanding of the relative strength and sign of the exchange coupling [44–47].

The total energy calculations show that the unique structural motif of YCMBO leads to quasi-1D magnetic behavior. The edge shared MnO_6 chains along the c -axis exhibit strong FM exchange coupling with an intra-chain exchange constant of ~ 2.3 meV ($J_c/k_B \simeq 26.7$ K), while the intra-plane exchange interaction is AFM and relatively weak (~ 0.25 meV, which is $J_{ab}/k_B \simeq 2.9$ K). Such a strong FM coupling is rare for Mn–O–Mn interactions, which in many oxides like MnO or LiMnBO_3 [48] is typically AFM in nature in the iso-electronic and iso-spin configurations in a Jahn–Teller distorted environment. According to the Goodenough-Kanamori rule, the

Mn-O-Mn super-exchange via 90° favors FM interaction for the d^4 high spin $S = 2$ systems [49]. A careful investigation of bond angles divulges that due to the distorted MnO_6 octahedra, the two $\angle\text{Mn-O-Mn}$ angles in YCMBO are $\sim 83.5^\circ$ and $\sim 102.4^\circ$ along the chain [48]. Notably, the oxygen atoms bridging Mn atoms along the chain exhibit substantial magnetic moments, with values of $-0.065/0.083 \mu_B$ and $0.055/0.059 \mu_B$ for short and long Mn-O-Mn bonds, respectively, in contrast to the negligible moment observed on oxygen atoms that connect adjacent chains. This spin polarization of the O atoms is a clear indication of strong Mn-O-Mn FM super-exchange interactions along the chains. Each linking oxygen atom, therefore, forms two bonds to adjacent Mn ions via either two half-occupied Mn dz^2 orbitals or two empty Mn $dx^2 - y^2$ orbitals [Fig. 8(b)(lower)]. Furthermore, the relatively short Mn-Mn distances within the chains, compared to those in the ab -plane, support the conclusion that intra-chain super-exchange is the dominant magnetic interaction pathway.

In contrast, the inter-chain interactions within the kagomé plane are geometrically frustrated. Due to the triangular coordination of magnetic ions, a fully compensated AFM arrangement cannot be simultaneously satisfied among all nearest neighbors, leading to a large ground-state degeneracy. The extremely small value of the intra-plane interactions suggests that the coupling arises from higher-order mechanisms such as super-super-exchange via B and O or dipolar interactions, both of which are suppressed by the in-plane frustration. Consequently, magnetic LRO only sets in below a relatively low temperature of approximately 7.8 K, adopting a $q = 0$ propagation vector consistent with the calculated results [24].

The magnetocrystalline anisotropy energy (MAE) was evaluated as the total energy difference between the spin quantization oriented along the [001] (out-of-plane) and [110] (in-plane) crystallographic directions, defined as $E_{001} - E_{110}$. The resulting MAE is ~ 33.18 meV, indicating that the [001] direction is energetically favored over the [110] direction. The negative value of the anisotropy energy thus implies a uniaxial anisotropy with the easy magnetization axis aligned along the out-of-plane [001] direction.

A comparative analysis with isostructural analogues reveals the unique nature of magnetic interactions in this Mn-based system. Compounds such as $\text{YCa}_3(\text{CrO})_3(\text{BO}_3)_4$ (Cr^{3+} , d^3) [21] and $\text{YCa}_3(\text{VO})_3(\text{BO}_3)_4$ (V^{3+} , d^2) [22, 23] exhibit dominant AFM interactions along their respective chains, with $\theta_{\text{CW}} \simeq -120$ K and -453 K, respectively, and show no evidence of long-range magnetic ordering down to the lowest measured temperatures, indicating significantly stronger magnetic frustration in those systems. In contrast, similar to gaufreyite, a natural mineral with the composition $\text{Ca}_4\text{Mn}_3\text{O}_3(\text{BO}_3)_3\text{CO}_3$, Mn-based $\text{YCa}_3(\text{MnO})_3(\text{BO}_3)_4$ exhibits a remarkable coexistence of FM chains and frustrated AFM 2D kagome lay-

ers, making it a promising candidate for exploring the interplay between structure, orbital physics, and low-dimensional magnetism [50].

F. Critical Analysis of Magnetization

According to the mean field model, magnetic isotherms (M vs H) recorded close to the transition temperature should follow [51],

$$H/M = a + bM^2, \quad (6)$$

where a and b are constants. The plot of M^2 vs H/M at different temperatures are generally known as the Arrott plots. They are widely used in ferromagnets for a precise estimation of the ferromagnetic transition temperature and to understand the nature of magnetic transition [51, 52]. The Arrott plots for YCMBO are shown in Fig. 9(a). According to the Banerjee criteria, one can determine the nature of a magnetic phase transition by analyzing the slope of the Arrott plots [53]. Positive slope indicates a second-order phase transition (SOPT), while a negative slope implies a first-order phase transition (FOPT). The observed positive slope for YCMBO over the entire temperature range [Fig. 9(a)] signifies SOPT. However, Arrott plots don't follow Eq. (6), as they are not linear, suggesting that the transition is non-mean field type.

In order to determine correct universality class of the phase transition, we adopted modified Arrott plots (MAPs), which are based on the Arrott-Noakes equation [54],

$$(H/M)^{1/\gamma} = A\epsilon + BM^{1/\beta}. \quad (7)$$

Here, A and B are constants, $\epsilon = \frac{T-T^*}{T^*}$ represents the reduced temperature, and γ and β are critical exponents. The critical exponents derived from MAPs should generally fall under one of the universality classes listed in Table II. To select the suitable model for YCMBO, we used the Relative Slope (RS) method given in Ref. [55]. Relative slope is defined as, $RS = S(T)/S(T^*)$. Here, $S(T)$ and $S(T^*)$ are the slopes of the linearly fitted lines in the high-field region of the MAPs at different temperatures and at the transition temperature, respectively. The selection of the most accurate model for the given sample is based on how closely the RS value approaches unity both above and below T^* for a particular model [55]. Figure 9(b) shows RS calculated considering different models for YCMBO. It is evident that the Tricritical Mean Field Model (TMFM) shows the least deviation from unity in both the regions, below and above T^* K.

Generally, MAPs plotted by an accurate model should be a set of parallel straight lines, and the line corresponding to the transition temperature will pass through origin [38, 56]. Figure 9(c) shows MAPs using the TMFM critical exponents, $\beta = 0.25$ and $\gamma = 1$. They are almost straight lines in the high-field region. A linear fit is done

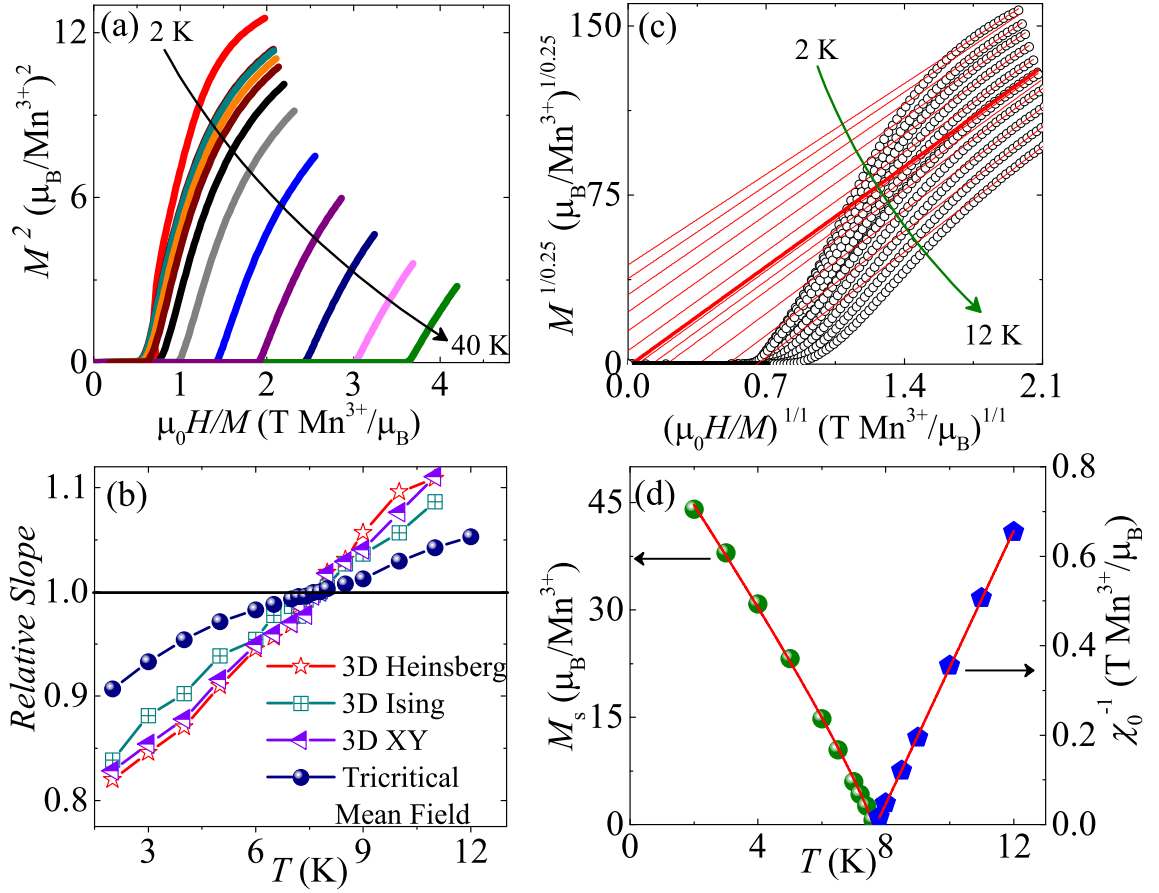


FIG. 9. (a) The Arrot plots at different temperatures near T^* . (b) Relative slope (RS) as a function of T for different models mentioned in Table II. (c) MAPs using the TMFM. The solid lines are the linear fits to data in high field regime. (d) Variation of spontaneous magnetization (M_s) and zero field inverse susceptibility (χ_0^{-1}) as function of T in left and right axes with solid lines as a fit using the Eq. (8) and (9), respectively.

in this range and extrapolated down to zero-field. It results in a set of parallel lines, and the line corresponding to $T_{\text{TMFM}} = 7.8$ K passes through origin [bold red line in Fig. 9(c)].

Generally, multiple iterations of MAPs are necessary to obtain reliable values of the critical exponents. For the next iteration, the values of β and γ are determined by the power law dependence of the critical exponent on the reduced temperature scale near the transition temperature as [56, 57],

$$M_S(T) = M_0(-\epsilon)^\beta \text{ for } \epsilon < 0, \quad (8)$$

and

$$\chi_0^{-1}(T) = \Gamma(\epsilon)^\gamma \text{ for } \epsilon > 0. \quad (9)$$

Here, M_S is the spontaneous magnetization and χ_0 is the zero field susceptibility. M_S and χ_0^{-1} are determined using the y -intercepts and x -intercepts of the extrapolated linear fits to the MAPs above and below the transition temperature, respectively. M_S and χ_0^{-1} obtained from Fig. 9(c) are plotted in Fig. 9(d). The solid lines in

Fig. 9(d) are fits to M_S and χ_0^{-1} using Eqs. (8) and (9), respectively. From these fits we got new values of $\beta' = 0.87$ and $\gamma' = 1$. By using these values, we have constructed new MAPs and performed a linear fit in the high-field region, and extrapolated the fits (not shown here). For $T > T_{\text{TMFM}}$, the x -intercepts are coming negative implying negative values of χ_0^{-1} . These unphysical values suggest the next interaction is not needed and the values obtained from first iteration, $\beta = 0.25$ and $\gamma = 1.00$ are the reliable values for YCMBO. Therefore, the accurate transition temperature of YCMBO according to this model is $T_{\text{TMFM}} \sim 7.8$ K. This value is close to the one obtained from magnetization and heat capacity data.

Further, critical exponent δ is calculated by using Widom relation given by [58],

$$\delta = 1 + \frac{\gamma}{\beta}. \quad (10)$$

Using the values of $\beta = 0.25$ and $\gamma = 1.00$, we obtained $\delta = 5$. These values of critical exponents for YCMBO align with the TCFM model when compared to all the universality classes given in Table II. Thus, we can con-

clude that YCMBO undergoes a magnetic transition at $T^* = T_{\text{TMFM}} \sim 7.8$ K and belongs to the TCMF universality class.

G. Magnetocaloric Effect

The magnetocaloric effect (MCE) is a property of magnetic materials where the temperature changes when subjected to the changing applied magnetic field. This is a useful property to achieve temperatures down to the milli-kelvin range. The protocol is to first apply a magnetic field to the sample isothermally and then remove the field slowly and adiabatically. The temperature of the sample is lowered in the second stage, and hence, this method is also widely known as adiabatic demagnetization refrigeration. In order to identify suitable materials for refrigeration, MCE is quantified by using two major parameters, change in isothermal entropy in the first stage (ΔS_m) and change in adiabatic temperature (ΔT_{ad}) in the second stage with respect to the change in applied field (ΔH).

We calculated ΔS_m separately by using magnetization isotherms and heat capacity data. In the first method, magnetization isotherms (M vs H) were recorded in close temperature steps in the vicinity of T^* . Then, Maxwell thermodynamic relation, $(\frac{\partial S}{\partial H})_T = (\frac{\partial M}{\partial T})_H$ is integrated to get

$$\Delta S_m(H, T) = \int_{H_i}^{H_f} \frac{dM}{dT} dH, \quad (11)$$

where, dM is the difference between the magnetization of two curves apart by temperature dT . The obtained ΔS_m as a function of temperature is shown in Fig. 10(a) for different values of $\Delta H = H_f - H_i$ from 1 T to 7 T. All the curves increase with temperature and show a broad maxima around 13 K. The maximum peak value of $\Delta S_m \simeq 12$ J/kg-K is observed for a field change of $\Delta H = 7$ T.

Further, to cross-check the values of ΔS_m , we have also done the calculations using field-dependent heat capacity data. First, the total entropy at a given field H is obtained by simply integrating $(C_p)_H$ as, $S(T)_H = \int_{T_i}^{T_f} \frac{(C_p)_H}{T} dT$. Next, ΔS_m is obtained by subtracting the zero-field entropy from the entropy at higher fields as,

$$\Delta S_m(T) = S(T)_H - S(T)_0. \quad (12)$$

Figure 10(b) presents the obtained ΔS_m as a function of temperature in different fields. The overall shape of the curve and maxima position are the same as obtained by the first method, with only a slight reduction in the peak values. The value of ΔS_m calculated using the heat capacity data is regarded to be more accurate than that obtained using the magnetization data [17]. The maximum value of ΔS_m obtained at 7 T is ~ 11 J/kg-K. Likewise, ΔT_{ad} is calculated by taking the difference in

temperature corresponding to the same entropy (adiabatic change) at two different applied fields as [17],

$$\Delta T_{\text{ad}} = T(S)_{H_f} - T(S)_{H_i}. \quad (13)$$

Figure 10(c) depicts the variation of ΔT_{ad} as a function of temperature. The maximum value of ΔT_{ad} is found to be around 8.4 K for $\Delta H = 7$ T.

As we got large values of MCE parameters, we also calculated one more figure of merit to determine the potential of YCMBO for magnetic refrigeration application, namely relative cooling power (RCP). RCP quantifies the amount of heat transfer between the cold and hot reservoirs in the refrigeration cycle, which can be expressed mathematically as

$$RCP = \int_{T_{\text{cold}}}^{T_{\text{hot}}} \Delta S_m(T, H) dT. \quad (14)$$

The approximated formula for RCP is given by

$$|RCP|_{\text{simeq}} = \Delta S_m^{\text{peak}} \times \delta T_{\text{FWHM}}, \quad (15)$$

where ΔS_m^{peak} is the peak value and δT_{FWHM} is full width half maxima of the ΔS_m vs T curves in Fig. 11(a). ΔS_m^{peak} and the calculated RCP as a function of field are shown in Fig. 11(a). The maximum value of RCP is obtained to be ~ 349 J/kg for 7 T.

For practical application of the material in magnetic cooling, large values of ΔS_m , ΔT_{ad} , and RCP are not only the necessary criteria. The nature of magnetic transition also plays a decisive role. For instance, materials with FOPT might have large peak heights of the ΔS_m curves, but their width is narrow. Also, these transitions are non-reversible and come with thermal hysteresis [63]. Due to these limitations, FOPT materials have less working range and efficiency in the cyclic processes of MCE. On the other hand, materials undergoing SOPT with a reversible nature and negligible hysteresis are more desirable. In order to examine the nature of the phase transition, we followed the method given in Ref. [56]. The plots of ΔS_m vs H for different temperatures near the transition are fitted by a power law, $\Delta S_m \propto H^n$ as shown in the inset of Fig. 11(b). The obtained n values as a function of temperature are plotted in Fig. 11(b). The value of n remains below 2, implying SOPT [35, 64].

Franco et. al. [65] proposed another method to determine the nature of the phase transition from the construction of universal scaling curve of ΔS_m . Universal scaling curve is constructed by plotting $\Delta S_m / \Delta S_m^{\text{peak}}$ (normalized ΔS_m) vs θ . Here, θ is the rescaled temperature axis. The rescaling is done as,

$$\theta = \begin{cases} -(T - T^*) / (T_{r1} - T^*), & T \leq T^* \\ -(T - T^*) / (T_{r2} - T^*), & T \geq T^* \end{cases} \quad (16)$$

where, T_{r1} and T_{r2} are two temperature extrema corresponding to half of ΔS_m^{peak} . If all the scaled curves collapse to a single curve (also known as the master or universal curve), that implies SOPT [66, 67]. Figure 11(c)

TABLE II. List of the critical exponents β , γ , δ , and T^* of YCMBO calculated from MAPs and theoretical values for different universality classes taken from Ref. [57].

Parameters	MAPs (YCMBO)	Tri Critical Mean field	Mean field model	3D Heisenberg model	3D XY model	3D Ising model
β	0.25	0.25	0.5	0.365	0.345	0.325
γ	1	1	1	1.386	1.316	1.241
δ	5	5	3	4.8	4.8	4.82
T^* (K)	7.8	-	-	-	-	-

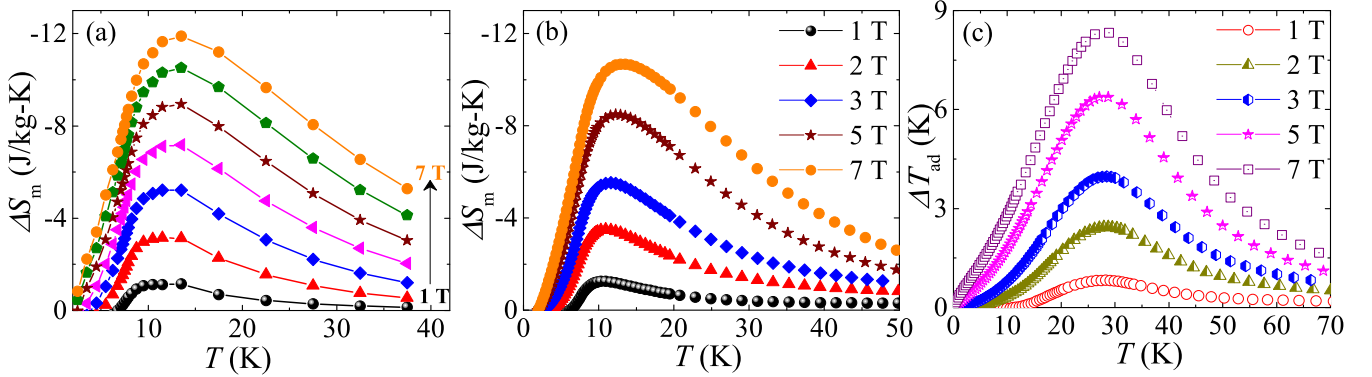


FIG. 10. (a) Isothermal magnetic entropy change (ΔS_m) as a function of T calculated at various applied fields using Eq. (11). (b) Variation of ΔS_m with T calculated using field-dependent heat capacity data and Eq. (12). (c) Adiabatic temperature change (ΔT_{ad}) as a function of T calculated at various applied fields using Eq. (13).

TABLE III. MCE parameters of YCMBO are compared with previously studied materials having T_C (or T_N) in the same temperature range. ΔH stands for the field change during the cooling cycle.

Compounds	T_C or T_N (K)	ΔH (T)	$ \Delta S_m^{\text{peak}} $ (J/kg-K)	RCP (J/kg)	Ref.
Tm ₂ FeCrO ₆	10.5 K	5	4.78	123.5	[59]
Er ₂ FeCr ₆	11.7/5.7 K	5	11.95	215.8	[59]
Er ₂ Ni ₂ Ga	7.1 K	7	12.93	265	[60]
HoMnO ₃	5 K	7	13.1	320	[61]
Tb ₃ RuO ₇	12 K	5	7.78	128.8	[62]
Gd ₃ RuO ₇	11 K	5	8.12	124	[62]
YCMBO	7.8 K	7	12	349	This work

presents the universal curve construction for YCMBO. All curves in different fields are nicely overlapping with each other, further confirming SOPT in YCMBO.

We have compared the MCE parameters of YCMBO with already reported MCE materials having the magnetic transition near to T^* in Table III. The MCE parameters of YCMBO are comparable to those of the other potential candidates. Additionally, it has a considerably large value of RCP , among the listed compounds. It is worth noting that YCMBO is the only rare earth-

free compound in Table III. YCMBO has three $S = 2$ magnetic Mn³⁺ ions having the potential to accommodate large zero-field entropy of about $S_m = 40$ J/mol K. Further, due to major FM interaction between the ions, we can observe considerable entropy change with a small change in magnetic field. The competing FM-AFM interaction near the transition causes the entropy to distribute over a large temperature range as reflected in broad ΔS_m vs T curves. Therefore, YCMBO gives rise to a substantial RCP value. With large MCE parameters, SOPT, and negligible hysteresis YCMBO is found to be yet another potential material for magnetic refrigeration.

IV. SUMMARY

In summary, we revisited the magnetic properties and studied the MCE character of YCMBO in detail. The kagome lattice compound undergoes a FM ordering at $T^* \simeq 7.8$ K with a spin canting due to competing FM and AFM interactions. A power law fit to C_{mag}/T below T^* gives an exponent $n \simeq 0.5$, indicative of a FM transition. Despite coexisting FM and AFM interactions, the frustration parameter ($f \simeq 4$) is found to be considerably large, a robust signature of strong frustration in the system. Band structure calculations confirm dominant FM interaction along the chain and weak AFM interaction in the kagome plane perpendicular to the chain

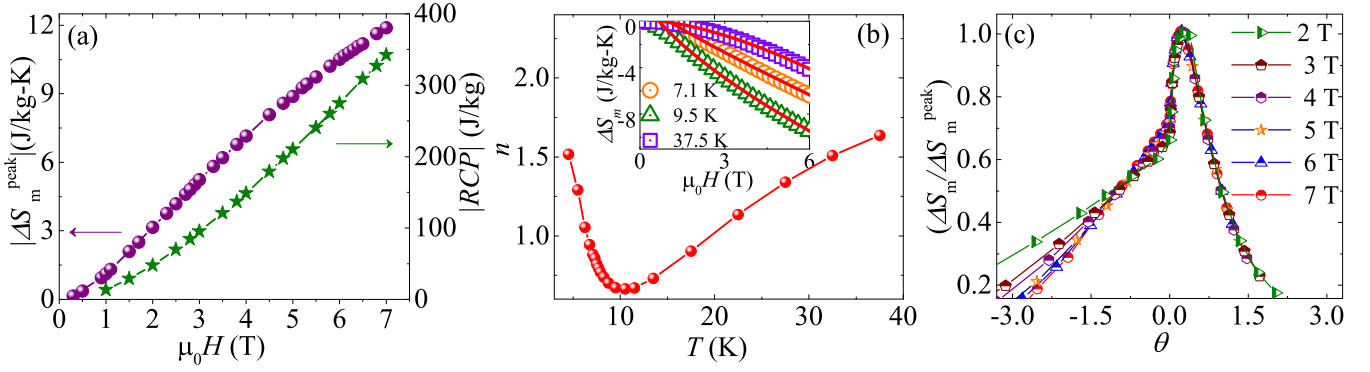


FIG. 11. (a) Field evaluation of ΔS_m^{peak} (left-axis) and RCP (right-axis). (b) The exponent n as a function of temperature, obtained from the fitting of power law to ΔS_m vs H isotherms. A few representative fits are shown in the inset for temperatures near and well above T_C . (c) Normalized magnetic entropy ($\Delta S_m / \Delta S_m^{\text{peak}}$) are plotted as a function of the rescaled temperature (θ) [Eq. (16)] in different fields.

direction. It exhibits a large MCE ($\Delta S_m \simeq 12$ J/kg-K, $\Delta T_{\text{ad}} \simeq 8.4$ K, and $RCP \simeq 349$ J/kg for $\Delta H = 7$ T.) comparable to other reported MCE materials having the transition temperature at around T^* . The critical analysis of magnetization via modified Arrott plots and MCE parameters establish SOPT at T^* and a tricritical mean field type FM with critical exponents $\beta = 0.25$, $\gamma = 1$, and $\delta = 5$. Being a rare-earth free compound, along with large MCE parameters, SOPT, and absence of magnetic hysteresis, YCMBO serves as an excellent material for

cooling purpose using ADR technique.

V. ACKNOWLEDGMENTS

For financial support, we would like to acknowledge SERB, India bearing sanction Grant No. CRG/2022/000997 and DST-FIST with Grant No. SR/FST/PS-II/2018/54(C).

-
- [1] C. Lacroix, P. Mendels, and F. Mila, *Introduction to Frustrated Magnetism: Materials, Experiments, Theory*, Springer Series in Solid-State Sciences (Springer Berlin Heidelberg, 2011).
 - [2] M. R. Norman, Colloquium: Herbertsmithite and the search for the quantum spin liquid, *Rev. Mod. Phys.* **88**, 041002 (2016).
 - [3] A. Olariu, P. Mendels, F. Bert, F. Duc, J. C. Trombe, M. A. de Vries, and A. Harrison, ^{17}O NMR Study of the Intrinsic Magnetic Susceptibility and Spin Dynamics of the Quantum Kagome Antiferromagnet $\text{ZnCu}_3(\text{OH})_6\text{Cl}_2$, *Phys. Rev. Lett.* **100**, 087202 (2008).
 - [4] A. S. Wills and A. Harrison, Structure and magnetism of hydronium jarosite, a model kagomé antiferromagnet, *J. Chem. Soc., Faraday Trans.* **92**, 2161 (1996).
 - [5] A. S. Wills, A. Harrison, S. A. M. Mentink, T. E. Mason, and Z. Tun, Magnetic correlations in deuterium jarosite, a model $S = 5/2$ Kagomé antiferromagnet, *EPL* **42**, 325 (1998).
 - [6] T. Inami, S. Maegawa, and M. Takano, Neutron-diffraction study on Na- and K-jarosites, *J. Am. Chem. Soc.* **177-181**, 752 (1998).
 - [7] T. Yildirim and A. B. Harris, Magnetic structure and spin waves in the Kagomé jarosite compound $\text{KFe}_3(\text{SO}_4)_2(\text{OH})_6$, *Phys. Rev. B* **73**, 214446 (2006).
 - [8] A. Keren, K. Kojima, L. P. Le, G. M. Luke, W. D. Wu, Y. J. Uemura, M. Takano, H. Dabkowska, and M. J. P. Gingras, Muon-spin-rotation measurements in the kagomé lattice systems: Cr-jarosite and Fe-jarosite, *Phys. Rev. B* **53**, 6451 (1996).
 - [9] D. Papoutsakis, D. Grohol, and D. G. Nocera, Magnetic Properties of a Homologous Series of Vanadium Jarosite Compounds, *J. Am. Chem. Soc.* **124**, 2647 (2002).
 - [10] S. Lee, T. Zhu, Y. Oshima, T. Shiroka, C. Wang, H. Luetkens, H. Yang, M. Lü, and K.-Y. Choi, Timescale distributions of spin fluctuations in the $S = 2$ kagome antiferromagnet $\text{CsMn}_3\text{F}_6(\text{SeO}_3)_2$, *Phys. Rev. B* **105**, 094439 (2022).
 - [11] D. Chen, C. Le, C. Fu, H. Lin, W. Schnelle, Y. Sun, and C. Felser, Large anomalous Hall effect in the kagome ferromagnet LiMn_6Sn_6 , *Phys. Rev. B* **103**, 144410 (2021).
 - [12] T. Asaba and V. Ivanov and S. M. Thomas and S. Y. Savrasov and J. D. Thompson and E. D. Bauer and F. Ronning, Colossal anomalous nernst effect in a correlated noncentrosymmetric kagome ferromagnet, *Sci. Adv.* **7**, eabf1467 (2021).
 - [13] S. Howard, L. Jiao, Z. Wang, N. Morali, R. Batabyal, P. Kumar-Nag, N. Avraham, H. Beidenkopf, P. Vir, E. Liu, C. Shekhar, C. Felser, T. Hughes, and V. Madhavan, Evidence for one-dimensional chiral edge states in a magnetic Weyl semimetal $\text{Co}_3\text{Sn}_2\text{S}_2$, *Nat. Commun.* **12**, 4269 (2021).
 - [14] A. Mook, J. Henk, and I. Mertig, Magnon Hall effect and topology in kagome lattices: A theoretical investigation, *Phys. Rev. B* **89**, 134409 (2014).

- [15] R. Chisnell, J. S. Helton, D. E. Freedman, D. K. Singh, F. Demmel, C. Stock, D. G. Nocera, and Y. S. Lee, Magnetic transitions in the topological magnon insulator $\text{Cu}(1,3\text{-bdc})$, *Phys. Rev. B* **93**, 214403 (2016).
- [16] R. Chisnell, J. S. Helton, D. E. Freedman, D. K. Singh, R. I. Bewley, D. G. Nocera, and Y. S. Lee, Topological Magnon Bands in a Kagome Lattice Ferromagnet, *Phys. Rev. Lett.* **115**, 147201 (2015).
- [17] A. Magar, K. Somesh, V. Singh, J. Abraham, Y. Senyk, A. Alfonso, B. Büchner, V. Kataev, A. Tsirlin, and R. Nath, Large Magnetocaloric Effect in the Kagome Ferromagnet $\text{Li}_9\text{Cr}_3(\text{P}_2\text{O}_7)_3(\text{PO}_4)_2$, *Phys. Rev. Appl.* **18**, 054076 (2022).
- [18] V. K. Pecharsky and K. A. Gschneidner Jr, Magnetocaloric effect and magnetic refrigeration, *J. Magn. Mater.* **200**, 44 (1999).
- [19] M.-H. Phan and S.-C. Yu, Review of the magnetocaloric effect in manganite materials, *J. Magn. Mater.* **308**, 325 (2007).
- [20] R. Li, G. Li, and C. Greaves, Gaufreyite: a mineral with excellent magnetocaloric effect suitable for liquefying hydrogen, *J. Mater. Chem. A* **6**, 5260 (2018).
- [21] C.-H. Wang, M. Avdeev, B. J. Kennedy, M. Küpers, and C. D. Ling, $\text{YCa}_3(\text{CrO})_3(\text{BO}_3)_4$: A Cr^{3+} Kagomé Lattice Compound Showing No Magnetic Order down to 2 K, *Inorg. Chem.* **55**, 7535 (2016).
- [22] H. J. Silverstein, R. Sinclair, A. Sharma, Y. Qiu, I. Heinmaa, A. Leitmäe, C. R. Wiebe, R. Stern, and H. Zhou, Naturally tuned quantum critical point in the $S = 1$ kagome $\text{YCa}_3(\text{VO})_3(\text{BO}_3)_4$, *Phys. Rev. Mater.* **2**, 044006 (2018).
- [23] W. Miiller, M. Christensen, A. Khan, N. Sharma, R. B. Macquart, M. Avdeev, G. J. McIntyre, R. O. Piltz, and C. D. Ling, $\text{YCa}_3(\text{VO})_3(\text{BO}_3)_4$: A Kagomé Compound Based on Vanadium(III) with a Highly Frustrated Ground State, *Chem. Mater.* **23**, 1315 (2011).
- [24] R. K. Li and C. Greaves, $\text{YCa}_3(\text{MnO})_3(\text{BO}_3)_4$: A manganese borate containing ferromagnetic chains on a kagomé lattice, *Phys. Rev. B* **68**, 172403 (2003).
- [25] G. Kresse and J. Hafner, Ab initio molecular dynamics for liquid metals, *Phys. Rev. B* **47**, 558 (1993).
- [26] G. Kresse and J. Furthmüller, Efficient iterative schemes for ab initio total-energy calculations using a plane-wave basis set, *Phys. Rev. B* **54**, 11169 (1996).
- [27] J. P. Perdew, K. Burke, and M. Ernzerhof, Generalized Gradient Approximation Made Simple, *Phys. Rev. Lett.* **77**, 3865 (1996).
- [28] J. P. Perdew, S. Kurth, A. c. v. Zupan, and P. Blaha, Accurate Density Functional with Correct Formal Properties: A Step Beyond the Generalized Gradient Approximation, *Phys. Rev. Lett.* **82**, 2544 (1999).
- [29] V. I. Anisimov, I. V. Solovyev, M. A. Korotin, M. T. Czyżyk, and G. A. Sawatzky, Density-functional theory and NiO photoemission spectra, *Phys. Rev. B* **48**, 16929 (1993).
- [30] S. L. Dudarev, G. A. Botton, S. Y. Savrasov, C. J. Humphreys, and A. P. Sutton, Electron-energy-loss spectra and the structural stability of nickel oxide: An LSDA+U study, *Phys. Rev. B* **57**, 1505 (1998).
- [31] D. Hobbs, G. Kresse, and J. Hafner, Fully unconstrained noncollinear magnetism within the projector augmented-wave method, *Phys. Rev. B* **62**, 11556 (2000).
- [32] W. Tang, E. Sanville, and G. Henkelman, A grid-based Bader analysis algorithm without lattice bias, *J. Phys. Condens. Matter* **21**, 084204 (2009).
- [33] E. Sanville, S. D. Kenny, R. Smith, and G. Henkelman, Improved grid-based algorithm for Bader charge allocation, *J. Comput. Chem.* **28**, 899 (2007).
- [34] Y. Savina, O. Bludov, V. Pashchenko, S. L. Gnatchenko, P. Lemmens, and H. Berger, Magnetic properties of the antiferromagnetic spin- $\frac{1}{2}$ chain system $\beta\text{-TeVO}_4$, *Phys. Rev. B* **84**, 104447 (2011).
- [35] S. Mohanty, A. Magar, V. Singh, S. S. Islam, S. Guchhait, A. Jain, S. M. Yusuf, A. A. Tsirlin, and R. Nath, Double magnetic transitions, complex field-induced phases, and large magnetocaloric effect in the frustrated garnet compound $\text{Mn}_3\text{Cr}_2\text{Ge}_3\text{O}_{12}$, *Phys. Rev. B* **109**, 134401 (2024).
- [36] R. Nath, A. A. Tsirlin, E. E. Kaul, M. Baenitz, N. Büttgen, C. Geibel, and H. Rosner, Strong frustration due to competing ferromagnetic and antiferromagnetic interactions: Magnetic properties of $M(\text{VO})_2(\text{PO}_4)_2$ ($M = \text{Ca}$ and Sr), *Phys. Rev. B* **78**, 024418 (2008).
- [37] M. J. Dzara, A. C. Campello, A. T. Breidenbach, N. A. Strange, J. E. Park, A. Ambrosini, E. N. Coker, D. S. Ginley, Y. S. Lee, R. T. Bell, and R. W. Smaha, Influence of the Rare Earth Cation on the Magnetic Properties of Layered $12\text{R-Ba}_4\text{M}^{4+}\text{Mn}_3\text{O}_{12}$ ($M = \text{Ce}, \text{Pr}$) Perovskites, *Chem. Mater.* **36**, 2810 (2024).
- [38] R. Kolay, Q.-P. Ding, Y. Furukawa, A. A. Tsirlin, and R. Nath, Magnetic properties of the double trillium lattice antiferromagnet $\text{KBaCr}_2(\text{PO}_4)_3$, *Phys. Rev. B* **110**, 224405 (2024).
- [39] E. Gopal, *Specific heats at low temperatures* (Springer Science and Business Media, 2012).
- [40] S. J. Sebastian, S. S. Islam, A. Jain, S. M. Yusuf, M. Uhlarz, and R. Nath, Collinear order in the spin- $\frac{5}{2}$ triangular-lattice antiferromagnet $\text{Na}_3\text{Fe}(\text{PO}_4)_2$, *Phys. Rev. B* **105**, 104425 (2022).
- [41] C. Hellberg, W. Pickett, L. Boyer, H. Stokes, and M. Mehl, Ab Initio Calculation of Spin Gap Behavior in CaV_4O_9 , *J. Phys. Soc. Jpn.* **68**, 3489 (1999).
- [42] V. V. Mazurenko, F. Mila, and V. I. Anisimov, Electronic structure and exchange interactions of $\text{Na}_2\text{V}_3\text{O}_7$, *Phys. Rev. B* **73**, 014418 (2006).
- [43] H. J. Xiang, E. J. Kan, S.-H. Wei, M.-H. Whangbo, and X. G. Gong, Predicting the spin-lattice order of frustrated systems from first principles, *Phys. Rev. B* **84**, 224429 (2011).
- [44] J. Sannigrahi, J. Sichelschmidt, B. Koo, A. Banerjee, S. Majumdar, and S. Kanungo, Microscopic investigation of low dimensional magnet $\text{Sc}_2\text{Cu}_2\text{O}_5$: combined experimental and ab initio approach, *J. Phys. Condens. Matter* **31**, 245802 (2019).
- [45] R. Roy and S. Kanungo, J_{eff} states in quasi-one-dimensional antiferromagnetic spin chain hexagonal iridates $\text{Sr}_3\text{M}(\text{IrO}_6)$ ($M = \text{Mg}, \text{Zn}, \text{Cd}$): An ab initio comparative perspective, *Phys. Rev. B* **109**, 085107 (2024).
- [46] R. Roy and S. Kanungo, Quasi-two-dimensional antiferromagnetism with large magnetocrystalline anisotropy in the half-filled square-planar iridate $\text{Cs}_2\text{Na}_2\text{IrO}_4$, *Phys. Rev. B* **108**, 155110 (2023).
- [47] S. Kanungo, B. Yan, C. Felser, and M. Jansen, Active role of nonmagnetic cations in magnetic interactions for double-perovskite Sr_2BO_6 ($B = \text{Y}, \text{In}, \text{Sc}$), *Phys. Rev. B* **93**, 161116 (2016).
- [48] R. K. Li, C. T. Chen, and C. Greaves, Magnetic order of LiMnBO_3 : A new type of chiral magnetic ground state,

- [Phys. Rev. B **66**, 052405 \(2002\)](#).
- [49] J. B. Goodenough, *Magnetism and the chemical bond* (Interscience, New York, 1963); J. Kanamori, Superexchange interaction and symmetry properties of electron orbitals, *J. Phys. Chem. Solids* **10**, 87 (1959).
 - [50] R. Li, P. Manuel, F. Orlandi, and C. Greaves, Magnetic ordering of the cryogenic magnetic cooling mineral gaufreyite, *J. Mater. Chem. A* **6**, 21149 (2018).
 - [51] A. Arrott, Criterion for Ferromagnetism from Observations of Magnetic Isotherms, *Phys. Rev.* **108**, 1394 (1957).
 - [52] H. E. Stanley, *Introduction to phase transitions and critical phenomena*, International Series of Monographs on Physics (Oxford University Press, 1987).
 - [53] B. Banerjee, On a generalised approach to first and second order magnetic transitions, *Phys. Lett.* **12**, 16 (1964).
 - [54] A. Arrott and J. E. Noakes, Approximate Equation of State For Nickel Near its Critical Temperature, *Phys. Rev. Lett.* **19**, 786 (1967).
 - [55] D. Mazumdar, K. Das, and I. Das, Study of magnetocaloric effect and critical exponents in polycrystalline $\text{La}_{0.4}\text{Pr}_{0.3}\text{Ba}_{0.3}\text{MnO}_3$ compound, *J. Appl. Phys.* **127**, 093902 (2020).
 - [56] V. Singh, P. Bag, R. Rawat, and R. Nath, Critical behavior and magnetocaloric effect across the magnetic transition in $\text{Mn}_{1+x}\text{Fe}_{4-x}\text{Si}_3$, *Sci. Rep.* **10**, 6981 (2020).
 - [57] S. S. Islam, V. Singh, K. Somesh, P. K. Mukharjee, A. Jain, S. M. Yusuf, and R. Nath, Unconventional superparamagnetic behavior in the modified cubic spinel compound $\text{LiNi}_{0.5}\text{Mn}_{1.5}\text{O}_4$, *Phys. Rev. B* **102**, 134433 (2020).
 - [58] B. Widom, Equation of State in the Neighborhood of the Critical Point, *J. Chem. Phys.* **43**, 3898 (1965).
 - [59] Z. Dong, Z. Wang, and S. Yin, Structural, magnetic and cryogenic magneto-caloric properties in $\text{RE}_2\text{FeCrO}_6$ (RE = Er and Tm) compounds, *Ceram. Int.* **46**, 26632 (2020).
 - [60] D. Guo, H. Li, and Y. Zhang, Magnetic Phase Transition and Magnetocaloric Effect in Ternary $\text{Er}_2\text{Ni}_2\text{Ga}$ Compound, *IEEE Trans. Magn.* **55**, 1 (2019).
 - [61] A. Midya, P. Mandal, S. Das, S. Banerjee, L. S. S. Chandra, V. Ganesan, and S. R. Barman, Magnetocaloric effect in HoMnO_3 crystal, *Appl. Phys. Lett.* **96**, 142514 (2010).
 - [62] N. He, P. Wang, J. Huang, X. Wang, Y. Zhang, L. Hu, L. Li, and M. Yan, Structural, magnetic and magnetocaloric properties in the rare earth ruthenate RE_3RuO_7 (RE = Pr, Nd, Gd and Tb) oxides with fluorite related structure, *Ceram. Int.* **48**, 36968 (2022).
 - [63] V. Franco, J. Blázquez, B. Ingale, and A. Conde, The Magnetocaloric Effect and Magnetic Refrigeration Near Room Temperature: Materials and Models, *Annu. Rev. Mater. Res.* **42**, 305 (2012).
 - [64] J. Y. Law, V. Franco, L. M. Moreno-Ramírez, A. Conde, D. Y. Karpenkov, I. Radulov, K. P. Skokov, and O. Gutfleisch, A quantitative criterion for determining the order of magnetic phase transitions using the magnetocaloric effect, *Nat. Commun.* **9**, 2680 (2018).
 - [65] V. Franco, J. S. Blázquez, and A. Conde, Field dependence of the magnetocaloric effect in materials with a second order phase transition: A master curve for the magnetic entropy change, *Appl. Phys. Lett.* **89**, 222512 (2006).
 - [66] C. M. Bonilla, F. Bartolomé, L. M. García, M. Parra-Borderías, J. Herrero-Albillos, and V. Franco, A new criterion to distinguish the order of magnetic transitions by means of magnetic measurements, *J. Appl. Phys.* **107**, 09E131 (2010).
 - [67] Q. Y. Dong, H. W. Zhang, J. R. Sun, B. G. Shen, and V. Franco, A phenomenological fitting curve for the magnetocaloric effect of materials with a second-order phase transition, *J. Appl. Phys.* **103**, 116101 (2008).